DTU Library

A New Virtual Inductance Control Method for Frequency Stabilization of Grid Forming Virtual Synchronous Generators

Yang, Yaqian; Xu, Jiazhu; Li, Chang; Zhang, Weiming; Wu, Qiuwei; Wen, Ming; Blaabjerg, Frede

Published in:
IEEE Transactions on Industrial Electronics

Link to article, DOI:
10.1109/TIE.2022.3148749

Publication date:
2022

Document Version
Peer reviewed version

A New Virtual Inductance Control Method for Frequency Stabilization of Grid-Forming Virtual Synchronous Generators

Yaqian Yang, Jiazhu Xu, *Member*, *IEEE*, Chang Li, Weiming Zhang, Qiuwei Wu, *Senior Member*, *IEEE*, Ming Wen, Frede Blaabjerg, *Fellow*, *IEEE*

***Abstract*—Frequency stabilization is the premise of guaranteeing grid-friendly integration of virtual synchronous generator (VSG). Based on that premise, this study, focused on frequency stability, establishes the small signal model of grid-forming VSG system. At first, the mechanism of frequency oscillation occurring in system of active- and reactive-power coupling is analyzed by the defined feedback effect factor (FEF) in this study. Besides, a new dynamic model is established for identifying dynamic interaction of voltage magnitudes and frequency by means of feedback effect. The analytical results of established models agree with that of eigenvalue analysis. Furthermore, a new virtual inductance control strategy is proposed to mitigate the unstable oscillation of frequency and powers, enhance damping performance, and improve stability margins. Unlike the conventional virtual inductance control, which is reliable on dual-loop control framework, the proposed virtual inductance control in this study is based on principle of energy conservation and can be applicable for the grid-forming inverter without inner dual-loop control structure. Finally, the proposed modeling as well as virtual inductance control method is experimentally verified.**

***Index Terms*—virtual synchronous generator (VSG), feedback effect, frequency stabilization, rate of change of frequency (RoCoF), frequency offset (FO), virtual inductance control**

I. Introduction

ENVIRONMENTAL pollution as well as energy crisis is getting more and more attentions. To cope with those issues, more and more distributed renewable energy generations are penetrating into modern power systems [1]. Low-inertia and poor-damping are remarkable characteristics of modern power systems due to the grid-integration of renewable energy. That characteristic directly leads to fast rate of change of frequency (RoCoF) and inevitable frequency nadir (FN) [2], which threatens secure operation of the AC power systems.

Virtual synchronous generator (VSG) control, which emulates the inertia and damping characteristics of conventional synchronous generator (SG), has been an emerging technique to improve inertia and damping of the system [3]. At present, the study of VSG are mainly focused on two aspects, i.e., control [4]-[7], and stabilization [8]-[16].

For example, a virtual inertia control strategy was proposed to provide inertia for AC power grid and improve FN [4]. However, this type of inertial control links DC voltage coupled with frequency, which is at the cost of drop of DC voltage. To rectify that drawback, a new compensator was proposed to alleviate the offset of DC voltage [5]. To overcome the shortcomings originated from fixed control parameters, an adaptive inertial control strategy was proposed to improve the stability of virtual synchronous machine (VSM) under various grid strengths [6]-[7]. Besides of this, an improved virtual inertia control was proposed to suppress frequency fluctuation of three-phase voltage source inverters [8]. No matter how the improved VSG control is implemented, the core idea is focused on the emulation of rotor swing equation of conventional SG. However, the premise that VSG provide inertia and damping support for the system is that VSG itself or grid-integration VSG system can maintain stable operation.

For example, a new modeling and parameters design methodology have been developed for VSG to guarantee secure operation of the system [9]. However, it is not involved in voltage stability or frequency stability. To fill in this gap, voltage and frequency stability analysis were discussed with a grid-forming VSG [10]. However, the proposed magnitude-phase motion equation (MPME) simplifies the model and does not consider the reactive power control coupling dynamics, which plays a predominant role in the system stability.

It was pointed out that grid-forming VSG can maintain good stability even when attaching to weak grid [13]-[14]. However, the stability mechanism is clarified from impedance model. The study in this paper shows that there is a risk of divergent oscillation appearing, when VSG is attached to power grid of resistance-inductance impedance, due to negative damping and positive feedback formed in the system. To fill in the gaps, this study builds a more complete MPME model to clarify the cause of frequency instability. Besides, the physical significance is

Yaqian Yang and Jiazhu Xu are with the Hunan University, Changsha 410082, China (*Corresponding author: Jiazhu Xu.*).

Chang Li and Qiuwei Wu are with Technical University of Denmark, Copenhagen, 2800, Denmark.

Weiming Zhang is with Shenzhen Power Supply Co., Ltd., Shenzhen, 518000, China.

Ming Wen is with the Economic Research Institute, State Grid Hunan Electric Power Company, Changsha, 410082, China.

Frede Blaabjerg is with Aalborg University, Aalborg, 9220, Denmark.

This article has been accepted for publication in a future issue of this journal, but has not been fully edited. Content may change prior to final publication. Citation information: DOI 10.1109/TIE.2022.3148749, IEEE Transactions on Industrial Electronics

discussed in various perspectives.

Although there have been several virtual impedance control strategies put forward to mitigate the oscillation of inverter or grid-forming VSG [15]-[17], all of them are realized by formulating the control links between current signal and voltage signal. However, dual-loop control structure is necessary for the implementation of virtual impedance. Therefore, to the best knowledge of the author, virtual impedance control is seldom proposed for grid-forming VSG without dual-loop control structure. Therefore, this study fills in the gaps.

The major contributions of this study are organized as follows:

1) Based on the established small signal modeling of grid-forming VSG system, the motion dynamics of both RoCoF and frequency offset (FO) can be judged by feedback effect. It is found that frequency stability of grid-forming VSG system is closely related with the transients of RoCoF and FO. And the feedback effect brought by internal relationship between RoCoF and FO gives physical insights to the frequency stability.

2) A new coupling model between voltage magnitude and frequency is established to clarify the feedback interaction between voltage and frequency of grid-forming VSG system, and the results of this analytical model agree with that of eigenvalue analysis.

3) A new virtual inductance control strategy is put forward to mitigate divergent oscillation of VSG frequency and powers, and enhance damping performance of the system. It should be noted that this type of virtual inductance is different from conventional virtual inductance control, which is dependent on the dual-loop control architecture. The proposed virtual inductance control is based on principle of energy conservations. It can be applied for VSG control structure without inner dual-loop control in this study. Besides, the effectiveness of the proposed virtual inductance control strategy is demonstrated by vector analysis and eigenvalue analysis.

4) The proposed control algorithm and methodology can be analogously applicable to DC systems, which is our present focus.

The remainders of this study are organized as follows: The next Section discusses mechanism analysis of frequency oscillation in grid-forming VSG system by the established small signal model. The dynamic behaviors of RoCoF and FO are studied by identifying feedback effect. And dynamic coupling model is established to clarify dynamic interaction between voltage magnitudes and frequency of VSG. Section III introduces the proposed virtual inductance control strategy to mitigate oscillation and improve damping performance. Section IV gives the experiments validations. Section V draws the conclusion.

II. MECHANISM ANALYSIS OF FREQUENCY OSCILLATION OF GRID-FORMING VSG

In this Section, mechanisms of both frequency oscillation and power coupling are discussed by the small signal modeling.

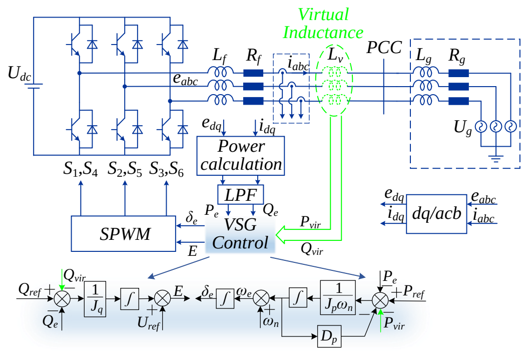

Fig. 1. Topology and control strategy of grid-forming VSG.

A. Power coupling model of grid-forming VSG system

In this part, small signal modeling is developed for analysis of frequency oscillation and power couplings. Fig. 1 shows the typical grid-forming VSG [10], which includes the topology and control strategy. L_v means introduced virtual inductance, which will be discussed in later Sections. As the DC link voltage is maintained by energy storage system, it is regarded as a constant value. The grid-forming VSG is connected to power grid via transmission lines and grid impedance. Total impedance of lines and grid is denoted as L_g and R_g. L_f and R_f represent the inductance and parasitic resistance of L filter, respectively. v_{abc} and i_{abc} are three-phase voltage at the point of common coupling (PCC) and the three-phase current through L-filter, respectively.

According to Fig. 1, the active- and reactive-power can be obtained in dq frame:

$$\begin{cases} P_e = \frac{3}{2}\left(e_d i_d + e_q i_q\right)\frac{\omega_L}{s+\omega_L} \\ Q_e = \frac{3}{2}\left(-e_d i_q + e_q i_d\right)\frac{\omega_L}{s+\omega_L} \end{cases} \quad (1)$$

where ω_L is the cutoff frequency of low pass filter, and the e_d, e_q, i_d, i_q are the voltage and current of d- and q-axis, respectively.

In dq frame, the voltage and current can be represented by:

$$\begin{cases} e_d = (R+Ls)i_d - \omega_n L i_q \\ e_q = \omega_n L i_d + (R+Ls)i_q \end{cases} \quad (2)$$

$$\begin{cases} i_d = \dfrac{(R+Ls)(E\cos\delta_e - U_g) + \omega_n LE\sin\delta_e}{(R+Ls)^2 + (\omega_n L)^2} \\ i_q = \dfrac{-\omega_n L(E\cos\delta_e - U_g) + (R+Ls)E\sin\delta_e}{(R+Ls)^2 + (\omega_n L)^2} \end{cases} \quad (3)$$

where R=R_f+R_g, L=L_f+L_g.

The VSG control dynamics, which emulates the inertia and damping of conventional SG, can be expressed as:

$$P_{ref} - P_e = D_p(\omega_e - \omega_n) + J_p\omega_n(\omega_e - \omega_n)s \quad (4.a)$$

$$Q_{ref} - Q_e = J_q(E - U_{ref})s \quad (4.b)$$

$$\delta_e = \frac{1}{s}\omega_e \quad (4.c)$$

where P_{ref}, Q_{ref} are the reference active- and reactive-power, P_e, Q_e are the output powers of the inverter. It should be noted that (4.a) and (4.c) mean frequency support for the system, and (4.b) represents voltage support for the system.

This article has been accepted for publication in a future issue of this journal, but has not been fully edited. Content may change prior to final publication. Citation information: DOI 10.1109/TIE.2022.3148749, IEEE Transactions on Industrial Electronics

Combing the equation of (1)-(3), the relationships among active power, reactive power, magnitudes and phase angle of output voltage of inverter can be written as:

$$P_e = f(\delta_e, E) \tag{5.a}$$

$$Q_e = g(\delta_e, E) \tag{5.b}$$

Linearizing Eq. (5) around the equilibrium points, one can obtain that:

$$\begin{cases} \Delta P_e = G_{P\delta}(s)\Delta\delta_e + G_{PE}(s)\Delta E \\ \Delta Q_e = G_{Q\delta}(s)\Delta\delta_e + G_{QE}(s)\Delta E \end{cases} \tag{6}$$

where $G_{P\delta}(s)$, $G_{PE}(s)$, $G_{Q\delta}(s)$, $G_{QE}(s)$ are the coupling terms between voltage magnitude as well as phase angle and powers. According to the developed small signal model, closed-loop control system of active power-frequency is shown in Fig. 2.

B. Dynamic Interactive Behavior and feedback effect between Frequency and Magnitude of VSG Output Voltage

According to Fig. 2, the internal relationship from ΔE to $\Delta\omega_e$ (ΔE divided by $\Delta\omega_e$) can be defined as $M_{\omega E}(s)$. Likewise, the relationship from $\Delta\omega_e$ to ΔE can be defined as $N_{E\omega}(s)$. By substituting (5.a) into (4.a) and combing (4.c), $M_{\omega E}(s)$ is derived by linearization:

$$M_{\omega E}(s) = \frac{\Delta\omega_e}{\Delta E} = \frac{-G_{PE}(s)/(J_p\omega_n s + D_p)}{\left[1 + G_{P\delta}(s)/(J_p\omega_n s^2 + D_p s)\right]} \tag{7}$$

Likewise, substituting (5.b) into (4.b), $N_{E\omega}(s)$ can be obtained as follows:

$$N_{E\omega}(s) = \frac{\Delta E}{\Delta\omega_e} = \frac{-G_{Q\delta}(s)/J_q s^2}{1 + G_{QE}(s)/J_q s} \tag{8}$$

It can be seen that Eq. (7) and Eq. (8) formulate the feedback loop to identify the dynamic interactions between frequency ($\Delta\omega_e$) and voltage magnitudes (ΔE). To more intuitively identify the dynamic interactive behavior between $\Delta\omega_e$ and ΔE, it is significant to define the i^{th} moment and the $(i+1)^{th}$ moment of the state variables, e.g., $\Delta\omega_e$ and ΔE. Provided that it is initial to define the i^{th} moment of $\Delta\omega_e$ as $\Delta\omega_{e\_i}$, thereby state of i^{th} moment of $\Delta E_{\_i}$ is dependent on the effect of $N_{E\omega}(s)$ with disturbance of $\Delta\omega_{e\_i}$. $\Delta E_{\_i}$ will in turn impose effect on state of $\Delta\omega_E$ through $M_{\omega E}(s)$. Therefore the state of $\Delta\omega_e$ will be accordingly updated, referred to as $\Delta\omega_{e\_i+1}$. Therefore, either positive feedback effect or negative feedback effect can be identified by comparing the updated state $\Delta\omega_{e\_i+1}$ with the earlier state $\Delta\omega_{e\_i}$. Moreover, the motion trajectory of VSG frequency can be judged by comparison between renewed state

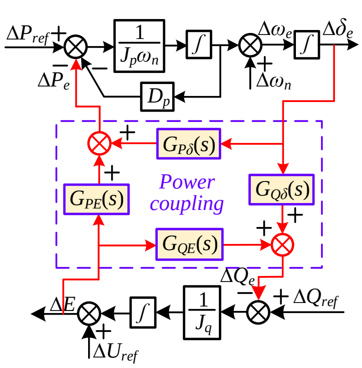

Fig. 2. Closed-loop control system of VSG system.

$\Delta\omega_{e\_i+1}$ and the original state $\Delta\omega_{e\_i}$. The coupling relationships between the renewed state and initial state can be described mathematically as follows:

$$\begin{cases} N_{E\omega}(s) = \dfrac{\Delta E_{\_i}}{\Delta\omega_{e\_i}} \\ M_{\omega E}(s) = \dfrac{\Delta\omega_{e\_i+1}}{\Delta E_{\_i}} \end{cases} \tag{9}$$

$$\Delta\omega_{e\_i+1} = M_{\omega E}(s)N_{E\omega}(s)\Delta\omega_{e\_i} = G_{MN}(s)\Delta\omega_{e\_i} \tag{10}$$

where $G_{MN}(s)$ is the transfer function which can depict the feedback effect on state variable $\Delta\omega_e$ and thus predict the motion trajectory of VSG frequency, i.e.,

$$G_{MN}(s) = \frac{G_{PE}(s)G_{Q\delta}(s)/\left[J_q s^2(J_p\omega_n s + D_p)\right]}{\left[1 + G_{P\delta}(s)/(J_p\omega_n s^2 + D_p s)\right](1 + G_{QE}(s)/J_q s)} \tag{11}$$

To better identify the motion state of VSG frequency, k is defined as feedback effect factor (FEF), i.e.,

$$\Delta\omega_{e\_i+1}\Big|_{\omega=\omega_{CFP}} = k\Delta\omega_{e\_i}\Big|_{\omega=\omega_{CFP}} \tag{12}$$

where the parameter k is the magnitude of $G_{MN}(s)$ at the critical frequency point (CFP). Thus k can be recalculated as:

$$k = 10^{\frac{A}{20}} \begin{cases} >1 & (A>0) \\ <1 & (A<0) \end{cases} \tag{13}$$

where A represents the magnitude of transfer function $G_{MN}(s)$ as the unit of Decibel (dB).

By rearranging Eq. (12), the RoCoF can be formulated as:

$$\begin{gathered} \frac{\Delta\omega_{e\_i+1}}{\Delta t} = k\frac{\Delta\omega_{e\_i}}{\Delta t} \\ \Downarrow \\ \frac{d\omega_{e\_i+1}}{dt} = k\frac{d\omega_{e\_i}}{dt} \end{gathered} \tag{14}$$

By considering (13), a unified expression is derived to clarify the dynamic characteristics of RoCoF, i.e.,

$$\frac{d\omega_{e\_n}}{dt} = k^n\frac{d\omega_{e\_0}}{dt} \tag{15}$$

$$\lim_{n\to+\infty} k^n = \begin{cases} +\infty & (k>1) \\ 0 & (k<1) \end{cases} \tag{16}$$

It can be seen in (16) that it forms positive feedback effect when $k>1$. And the RoCoF gets greater and greater, indicating that divergent oscillation appears in the system. It is because that divergence oscillation of frequency indicates both RoCoF and FO get larger and larger periodically. Vice versa, it forms negative feedback effect when $k<1$. And the oscillation will be dampened and frequency gets convergent to an equilibrium point.

In addition, the FO ($\delta\omega_e$) is defined as the frequency difference between the VSG frequency and the grid frequency, and the i^{th} FO can be derived as shown:

$$\delta\omega_{e\_i} = \sum_{i=0}^{i-1}\int_{t_i}^{t_{i+1}}\frac{d\omega_e}{dt}dt \qquad (i = 0,1,2\cdots n\cdots+\infty) \tag{17}$$

Another index to identify frequency stability is Relative Frequency Offset (RFO). For any positive integers i, j and $i>j$, if RFO ($R\omega_e$) is greater than zero, thereby the VSG frequency

This article has been accepted for publication in a future issue of this journal, but has not been fully edited. Content may change prior to final publication. Citation information: DOI 10.1109/TIE.2022.3148749, IEEE Transactions on Industrial Electronics

will be divergent and cannot return back to equilibrium point due to positive feedback effect, and vice versa.

$$R\omega_e = \delta\omega_{e\_i} - \delta\omega_{e\_j} \qquad (i>0, j>0, i>j) \tag{18}$$

According to the above discussions, FEF (k) imposes a great effect on the motion trajectory of RoCoF and RFO. The FO gets larger and larger when FEF>1 that forms a positive feedback effect. However, FO gets smaller and smaller when FEF<1, and negative feedback effect is formed to stabilize VSG frequency.

To validate the proposed modeling, Fig. 3 obtains the results of eigenvalue analysis and bode diagram of $G_{MN}(s)$ with different R_g. The system parameters are shown in Table I. In Fig. 3(a), the dominant eigenvalues are moving from left-half plane towards to the right-half plane as R_g gets enlarged, which indicates that the greater size of R_g is poorer for the stability of the system and has a larger risk of sub-synchronous oscillation. Fig. 3(b) shows bode diagram of $G_{MN}(s)$, from which it can be seen that a smaller R_g means lower magnitude of FEF. The lower magnitude of FEF means lower risk of positive feedback effect, and this will improve stability margins of the system. It can be inferred that smaller R_g can make the system more stable, and frequency stability is enhanced. According to the analysis of (14) and (16)-(18), it forms a negative feedback effect when FEF is below 1 (0 dB). And in this case, both RoCoF and FO are declined over time and gradually tend to be zero with the negative feedback effect. Therefore, it can be inferred that it forms a negative feedback when R_g=0.8 Ω.

However, the magnitude of $G_{MN}(s)$ is greater than zero at the CFP when R_g=1.2 Ω and R_g=1.6 Ω, divergent oscillation (instability) of active power and frequency will appear. Therefore, the proposed modeling with feedback effect is well illustrated by bodes analysis and eigenvalues.

TABLE I SYSTEM SPECIFICATIONS

Parameters	Symbol	Value
Rated active power	P_n	5 kW
Rated reactive power	Q_n	0 Var
DC voltage	U_{dc}	700 V
Filter inductance	L_f	4.4 mH
Resistance	R_f	0.1 Ω
Grid voltage	U_g(RMS)	380 V
Sampling frequency	f_s	10 kHz
Rated frequency	ω_n	314 rad/s
Inertia of Active Power	J_p	0.01
Damping coefficient	D_p	172.7
Inertia of Reactive Power	J_q	5

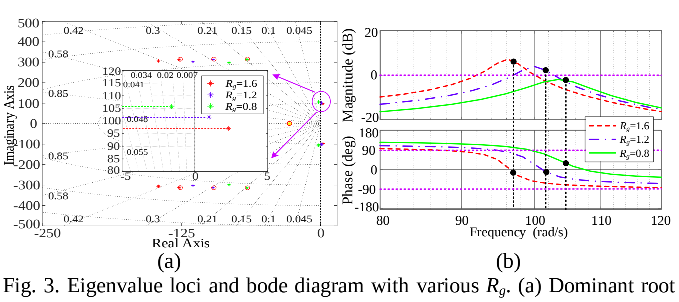

Fig. 3. Eigenvalue loci and bode diagram with various R_g. (a) Dominant root locus, (b) $G_{MN}(s)$.

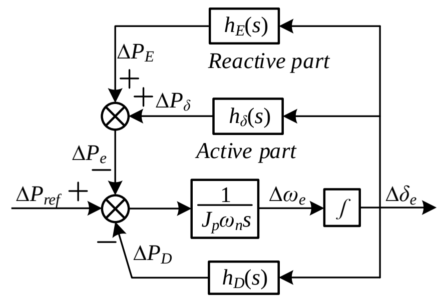

Fig. 4. Active power closed-loop transfer function block diagram.

To further discuss the frequency dynamics as well as system stability, by considering Eq. (6), (8) and Fig. 2, an active power closed-loop control diagram is shown in Fig. 4. The whole feedback paths include three parts, i.e., power-angle-related part (PARP) ($h_\delta(s)$), voltage-coupling-related part (VCRP) ($h_E(s)$) and damping part ($h_D(s)$). The outputs of the three feedback loops can be regarded as three equivalent active powers (i.e., ΔP_δ, ΔP_E, and ΔP_D) that interact with the virtual rotor, as depicted in Fig. 4. The dynamic behaviors of the virtual rotor are determined by the composite power (i.e., $\Delta P_\Sigma = \Delta P_\delta + \Delta P_E + \Delta P_D$), which can be used to evaluate the stability of the system.

Dynamic behaviors of system can be seen as superposition of dynamics of the feedback powers of three items, i.e.,

$$\Delta P_\Sigma = \underbrace{h_\delta(s)\Delta\delta_e}_{\Delta P_\delta} + \underbrace{h_E(s)\Delta\delta_e}_{\Delta P_E} + \underbrace{h_D(s)\Delta\delta_e}_{\Delta P_D} \tag{19}$$

where the transfer functions $h_\delta(s)$, $h_E(s)$ and $h_D(s)$ are given by:

$$\begin{cases} h_\delta(s) = \dfrac{\Delta P_\delta}{\Delta\delta_e} = G_{P\delta}(s) \\ h_E(s) = \dfrac{\Delta P_E}{\Delta\delta_e} = \dfrac{\Delta P_E}{\Delta E} * \dfrac{\Delta E}{\Delta\omega_e} * \dfrac{\Delta\omega_e}{\Delta\delta_e} = \dfrac{-G_{Q\delta}(s)G_{PE}(s)/J_q s}{1+G_{QE}(s)/J_q s} \\ h_D(s) = \dfrac{\Delta P_D}{\Delta\delta_e} = D_p s \end{cases} \tag{20}$$

The amplitude and phase of three transfer functions at critical frequency point can be derived, and accordingly, the vector diagrams of the active powers are carried out to investigate the stability of the system. It should be emphasized that Fig. 5(a), (b) show the results of transfer functions of $h_\delta(s)$, $h_E(s)$, and $h_D(s)$ with R_g=0.8 Ω and R_g=1.2 Ω, respectively. Fig. 5(c), (d) presents the corresponding vectors diagram. ΔP_δ, ΔP_E, ΔP_D, and ΔP_Σ represent PARP, VCRP, damping part, and total power [18].

Note that the phase of total active power at CFP is the focus of this paper. As for synchronous machine, the feedback active power can be divided into two items: damping power and synchronizing power, which are proportional to $\Delta\omega_e$ and $\Delta\delta_e$, separately. That vectors which are in the first quadrant means that the system is stable because of positive damping power and synchronizing power. From Fig. 5(c), the synthetic vector is located in the fourth quadrant with R_g=1.2 Ω. By decomposing the synthetic power ΔP_Σ into damping and synchronizing ones, the negative damping power exists, which will trigger the oscillation instability. Different from Fig. 5(c), Fig. 5(d) shows the synthetic vector ΔP_Σ, which provides positive damping to suppress the frequency oscillation and compel the system

This article has been accepted for publication in a future issue of this journal, but has not been fully edited. Content may change prior to final publication. Citation information: DOI 10.1109/TIE.2022.3148749, IEEE Transactions on Industrial Electronics

frequency convergent to an equilibrium point. It can be inferred that the grid resistance plays an important role in the stability of the system. Besides, greater grid resistance indicates the stronger coupling effect between active- and reactive-power, which will aggravate stability of grid-forming VSG.

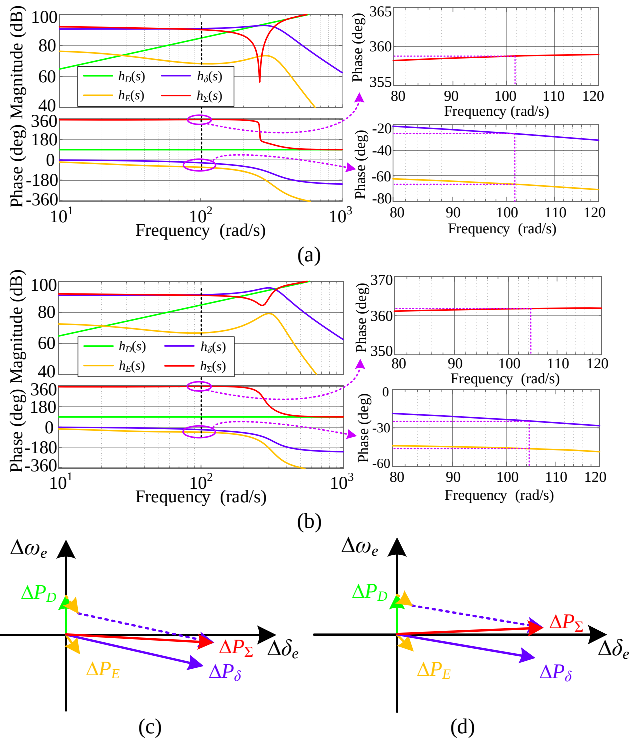

Fig. 5 Bode diagrams of $h_\delta(s)$, $h_E(s)$, $h_D(s)$, $h_\Sigma(s)$ and the corresponding vector diagram. (a) R_g=1.2 Ω, (b) R_g=0.8 Ω. (c) Corresponding vector diagram of (a). (d) Corresponding vector diagram of (b).

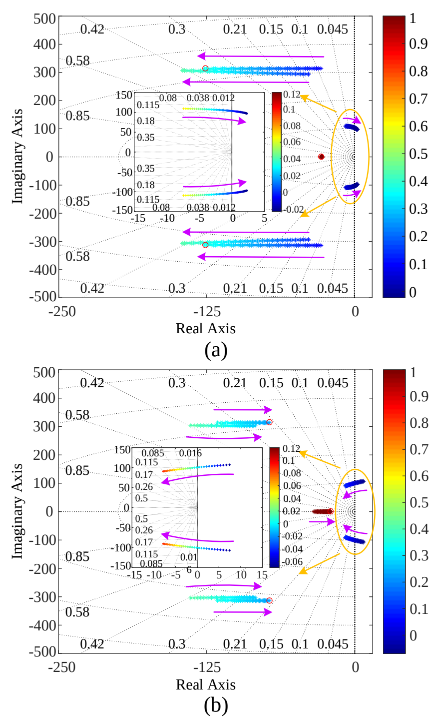

Fig. 6 Root locus of the studied system considering various R_g and L_g, (a) R_g changing from 0.3 to 1.6 Ω, (b) L_g varying from 6.6 to 13.2 mH

C. Influence of grid parameters on power stability and frequency oscillation

To reveal the influence of grid parameters on stability of grid-forming VSG system, eigenvalues with various R_g and L_g is developed in Fig. 6. From Fig. 6(a), the eigenvalues movement with R_g gradually increased from 0.3 to 1.6 Ω with L_g chosen as 8.8 mH. It can be seen that the coupling effect between active- and reactive-power becomes ever-increasing stronger. From partial enlarged view, a pair of dominant eigenvalues moves from the left half-plane to right half-plane, eventually arrives at unstable regions. Eigenvalue analysis results coincide with that of vector analysis. Fig. 6(b) shows the root locus with variations of L_g from 6.6 to 13.2 mH with R_g=1.2 Ω. The dominant eigenvalues move towards to the left half-plane as L_g gets greater, which indicates that the greater size of L_g enhance the stability of grid-forming VSG. In general, no matter increasing L_g or decreasing R_g aims to lessen coupling effect between active- and reactive-power, which can improve stability margins of the system.

III. Proposed Virtual Inductance Control Strategy for Mitigation of Frequency Oscillation of Grid-Forming VSG

In this section, a virtual inductance feed-forward control is proposed to enhance the stability of grid-forming VSG system, thereby frequency oscillation of grid-forming VSG is mitigated by the virtual inductance control as well.

A. Operation principle of virtual inductance control

As discussed earlier, increase of inductance alleviates the coupling effect between active- and reactive-power. In order to achieve good dynamic behavior, a virtual inductance, which emulates the real inductance, is developed. It should be noted that the virtual inductance is implemented by the control loop, which does not add hardware costs. Besides, the principle as well as architecture of virtual inductance is different from that in [19], [20], since that no architecture of dual-loop control is contained in this type of VSG. The equivalent power with consideration of virtual inductance can be rewritten as:

$$\begin{cases} P_{\_L_v} = \dfrac{3}{2}(e_{d\_L_v} i_{d\_L_v} + e_{q\_L_v} i_{q\_L_v}) \dfrac{\omega_L}{s+\omega_L} \\ Q_{\_L_v} = \dfrac{3}{2}(-e_{d\_L_v} i_{q\_L_v} + e_{q\_L_v} i_{d\_L_v}) \dfrac{\omega_L}{s+\omega_L} \end{cases} \tag{21}$$

where i_{d_Lv}, i_{q_Lv} is the *d*- and *q*-axis current with introduction of virtual inductance, i.e.,

$$\begin{cases} i_{d\_L_v} = \dfrac{[R+(L_v+L)s](E\cos\delta_e - U_g) + \omega_n (L_v+L) E \sin\delta_e}{[R+(L_v+L)s]^2 + [\omega_n (L_v+L)]^2} \\ i_{q\_L_v} = \dfrac{-\omega_n (L_v+L)(E\cos\delta_e - U_g) + [R+(L_v+L)s] E \sin\delta_e}{[R+(L_v+L)s]^2 + [\omega_n (L_v+L)]^2} \end{cases} \tag{22}$$

Based on the energy conservation, the difference of powers between with virtual inductance and without virtual inductance can be derived as:

$$\begin{cases} P_{vir} = P_{\_L_v} - P_e = m(\delta_e, E) \\ Q_{vir} = Q_{\_L_v} - Q_e = n(\delta_e, E) \end{cases} \tag{23}$$

This article has been accepted for publication in a future issue of this journal, but has not been fully edited. Content may change prior to final publication. Citation information: DOI 10.1109/TIE.2022.3148749, IEEE Transactions on Industrial Electronics

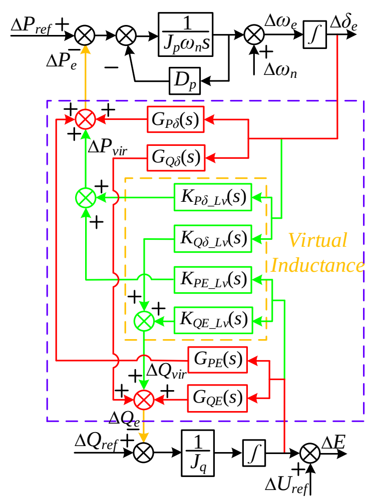

Fig. 7. Small signal diagram closed loop system of grid-forming VSG with virtual inductance control.

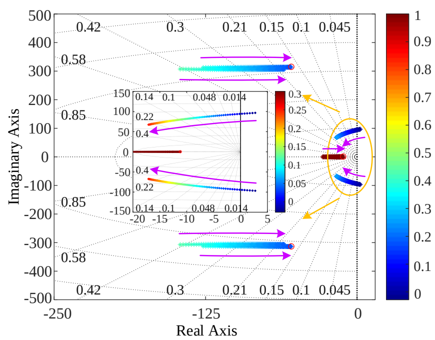

Fig. 8. Root locus diagram of the system with virtual inductance L_v varying from 0 to 17.6 mH.

Linearizing (23) yields (24)

$$\begin{cases}\Delta P_{vir}=K_{P\delta\_L_v}(s)\Delta\delta_e+K_{PE\_L_v}(s)\Delta E\\ \Delta Q_{vir}=K_{Q\delta\_L_v}(s)\Delta\delta_e+K_{QE\_L_v}(s)\Delta E\end{cases} \tag{24}$$

where ΔP_{vir} and ΔQ_{vir} represent the control instructions feed into the active-power control loop and reactive-power control loop, respectively.

Therefore, effect of virtual inductance can be realized by the derived control blocks in (24), as shown in Fig. 7.

B. Discussion on virtual inductance to dampen frequency oscillation

This part explores the principle of virtual inductance for damping frequency oscillation of the system. Besides, it shows the positive damping effect brought by the proposed virtual inductance control method.

Fig. 8 shows the eigenvalue analysis result with virtual inductance varying from 0 to 17.6 mH. Critical oscillatory modes move toward to the left half-plane as virtual inductance gets enlarged. It indicates that increase of virtual inductance can strengthen damping performance and enhance the system stability.

Analogous to (7) and (8), the relationship between $\Delta\omega_e$ and ΔE, with introducing virtual inductance, can be reformulated as:

$$M_{\omega E\_vir}(s)=\frac{\Delta\omega_{e\_vir}}{\Delta E_{\_vir}}=\frac{-[G_{PE}(s)+K_{PE\_Lv}(s)]}{J_p\omega_n s+D_p+[G_{P\delta}(s)+K_{P\delta\_Lv}(s)]/s} \tag{25}$$

$$N_{E\omega\_vir}(s)=\frac{\Delta E_{\_vir}}{\Delta\omega_{e\_vir}}=\frac{-[G_{Q\delta}(s)+K_{Q\delta\_Lv}(s)]/s}{J_q s+G_{QE}(s)+K_{QE\_Lv}(s)} \tag{26}$$

Therefore, replacing the relationship between $\Delta\omega_{E\_i+1}$ and $\Delta\omega_{E\_i}$ in (27), one can derive that:

$$G_{MN\_vir}(s)=M_{\omega E\_vir}(s)N_{E\omega\_vir}(s) \tag{27}$$

Fig. 9 displays the frequency response result of $G_{MN\_vir}(s)$ with changing various virtual inductances. The magnitude of $G_{MN\_vir}(s)$ is greater than 0 dB when L_v=0. It means that system loses stabilization in this case, and it forms a positive feedback effect that will destabilize frequency. However, as the virtual inductance L_v adding, the magnitude of $G_{MN\_vir}(s)$ is always below 0 dB, which ensures good stability margin of the system. In addition, it can be inferred that greater virtual inductance makes system more robust, and the negative feedback effect brought by virtual inductance gets stronger.

C. Physical significance of proposed virtual inductance control for mitigation of system oscillation

According to the above discussions, negative damping as well as positive feedback effect of the system is the predominant cause of divergence of system frequency. Hence, this part will introduce physical significance of the proposed virtual inductance for mitigation of system oscillation.

From the view of attributes of the powers, the feedback active power with consideration of virtual inductance can be divided into two parts, $h_{vir\_\delta}(s)$ and $h_{vir\_E}(s)$, i.e.,

$$\begin{cases}h_{vir\_\delta}(s)=\dfrac{\Delta P_{vir\_\delta}}{\Delta\delta_e}=K_{P\delta\_Lv}\\ h_{vir\_E}(s)=\dfrac{\Delta P_{vir\_E}}{\Delta\delta_e}=[G_{P\delta}(N_{E\omega\_vir}-N_{E\omega})+K_{P\delta\_Lv}N_{E\omega\_vir}]/s\end{cases} \tag{28}$$

Fig. 10 plots the frequency response results of $h_{vir\_\delta}(s)$ and $h_{vir\_E}(s)$ with various sizes of virtual inductance L_v (L_{v1}=4.4 mH, L_{v2}=8.8 mH, L_{v3}=13.2 mH, L_{v4}=17.6 mH). It can be seen that the magnitude of $h_{vir\_\delta}(s)$ is higher than that of $h_{vir\_E}(s)$ in the

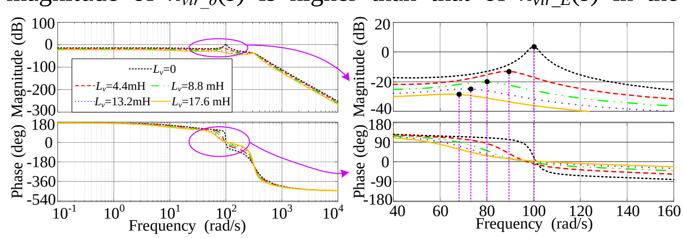

Fig. 9. Frequency responses of $G_{MN\_vir}(s)$ with different virtual inductances.

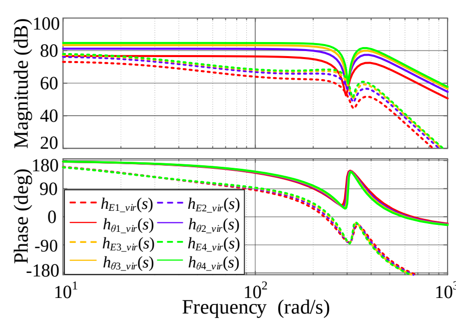

Fig.10. Bode diagrams of virtual active power in two parts with different L_v.

This article has been accepted for publication in a future issue of this journal, but has not been fully edited. Content may change prior to final publication. Citation information: DOI 10.1109/TIE.2022.3148749, IEEE Transactions on Industrial Electronics

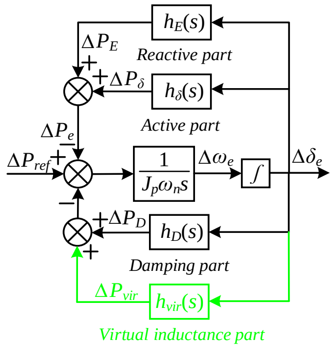

Fig.11. Active power closed-loop transfer function block diagram with virtual inductance.

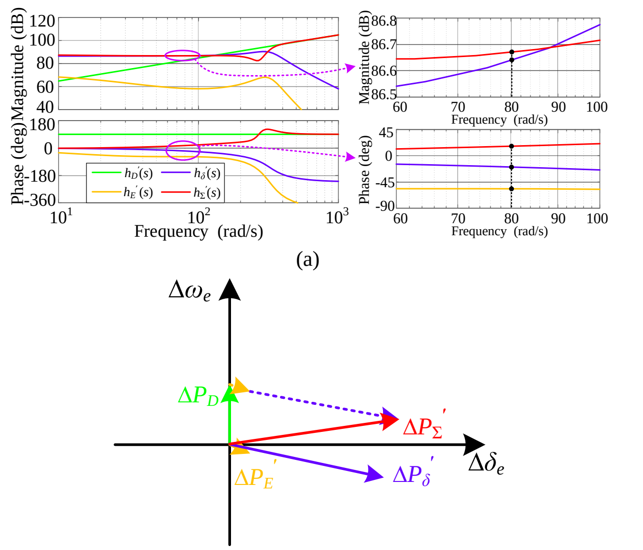

Fig. 12. Frequency responses of feedback power transfer functions and the corresponding vector diagram with L_v=8.8 mH, (a) frequency response, (b) vector illustration

selected frequency range, no matter what size of L_v, which illustrates that $h_{vir\_\delta}(s)$ plays a dominant role in stabilization of the system. The synthetic active power-angle transfer function with virtual inductance can be calculated by:

$$h_{vir}(s)=h_{vir\_\delta}(s)+h_{vir\_E}(s) \tag{29}$$

The small signal control system with virtual inductance control is presented as shown in Fig. 11. Therefore, the synthetic powers can be derived as:

$$\Delta P_\Sigma'=\underbrace{h_\delta(s)\Delta\delta_e}_{\Delta P_\delta}+\underbrace{h_E(s)\Delta\delta_e}_{\Delta P_E}+\underbrace{h_D(s)\Delta\delta_e}_{\Delta P_D}+\underbrace{h_{vir}(s)\Delta\delta_e}_{\Delta P_{vir}} \tag{30}$$

In order to illustrate how the virtual inductance impacts the dynamics of active power, the newly formed three feedbacks active powers are formulated as:

$$\begin{cases} h_\delta'(s)=\dfrac{\Delta P_\delta'}{\Delta\delta_e}=G_{P\delta}(s)+K_{P\delta\_Lv}(s) \\ h_E'(s)=\dfrac{\Delta P_E'}{\Delta\delta_e}=\dfrac{-\left(G_{Q\delta}(s)+K_{Q\delta\_Lv}(s)\right)\left(G_{PE}(s)+K_{PE\_Lv}(s)\right)}{J_q s+\left(G_{QE}(s)+K_{QE\_Lv}(s)\right)} \\ h_D'(s)=\dfrac{\Delta P_D'}{\Delta\delta_e}=D_p s \end{cases} \tag{31}$$

Consequently, (30) can be rearranged as:

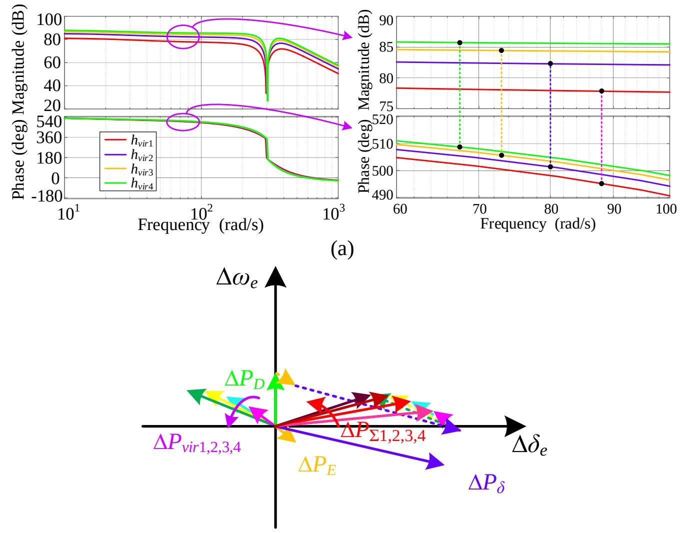

Fig. 13. Frequency responses and vector plot of the four active power feedback parts with different virtual inductance. (a) Frequency responses of $h_{vir}(s)$. (b) Vector diagram of active power components of ΔP_δ, ΔP_E, ΔP_D, ΔP_{vir} and ΔP_Σ.

$$\Delta P_\Sigma'=\underbrace{h_\delta'(s)\Delta\delta_e}_{\Delta P_\delta'}+\underbrace{h_E'(s)\Delta\delta_e}_{\Delta P_E'}+\underbrace{h_D'(s)\Delta\delta_e}_{\Delta P_D'} \tag{32}$$

Fig. 12 shows the frequency responses of $h_\delta'(s)$, $h_D'(s)$, $h_E'(s)$, $h_\Sigma'(s)$ and vector diagrams, which reflects the impact of virtual inductance on dynamic behavior of the grid-forming VSG system. Vectors are characterized by information of phase and magnitude at CFP. The synthetic power is located in the first quadrant, which illustrates the proposed virtual inductance control provides damping support for the system. Besides, negative damping power caused by strong power coupling effect can be offset by the effect of virtual inductance.

Fig. 13 shows the results of bodes as well as vector diagrams with varying size of virtual inductance (L_{v1}=4.4 mH, L_{v2}=8.8 mH, L_{v3}=13.2 mH, L_{v4}=17.6 mH). It shows that the greater virtual inductance results in stronger damping effect and negative feedback effect that can stabilize system. The effectiveness of the proposed virtual inductance control is reflected. Thereby the frequency stability is enhanced by the virtual inductance control.

IV. Simulation and Experiment Results

To verify the effectiveness of the proposed virtual inductance control method, Scenarios in different value of virtual inductance are built. Simulation results of frequency characteristic are displayed in Fig. 14. The attenuation speeds of the frequency with virtual inductance being 8.8 mH are much faster than that of virtual inductance being 4.4 mH. It inferred that the larger size of virtual inductance can make the

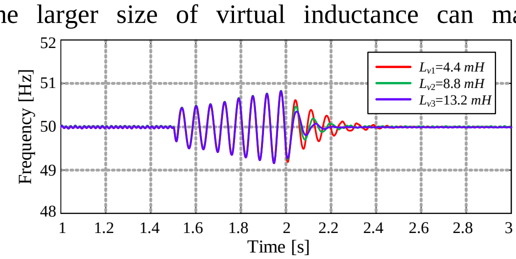

Fig. 14. Simulation results of the frequency with different virtual inductance.

This article has been accepted for publication in a future issue of this journal, but has not been fully edited. Content may change prior to final publication. Citation information: DOI 10.1109/TIE.2022.3148749, IEEE Transactions on Industrial Electronics

oscillation attenuated much faster and provide stronger damping for the system.

Specifically, the stability as well as dynamic performance of the grid-forming VSG (GFVSG) in this study is not only related with the short circuit ratio (SCR), but also concerned with the ratio of R_g/X_g. As can be seen in Fig. 15(a) and Fig. 15(c), higher level of R_g/X_g leads to poorer stability of the system with weaker damping performance. The oscillation in Fig. 15(a) is divergent, but oscillation in Fig. 15(c) is convergent due to the different R_g/X_g, but the dynamic characteristics are all improved with the proposed virtual inductance control in Fig. 15(b) and (d). Generally, in all of the case studies, the proposed virtual inductance can take good effect in suppressing oscillation with larger inertia and stronger damping.

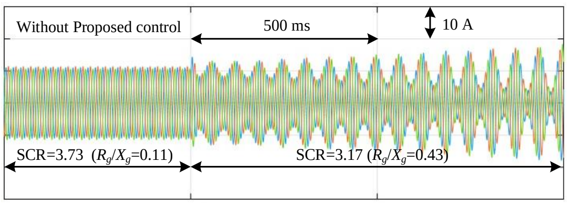

(a)

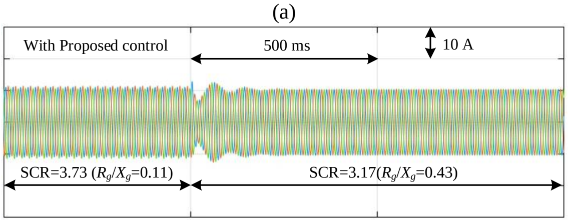

(b)

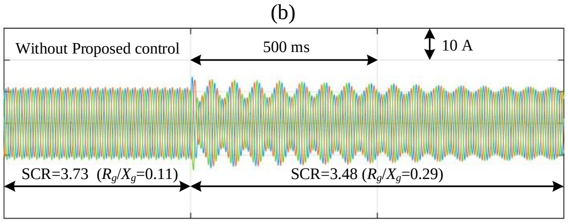

(c)

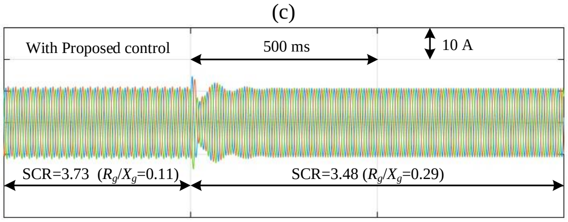

(d)

Fig. 15. Current response with and without proposed control. (a) Without proposed control (R_g/X_g=0.43), (b) With proposed control (R_g/X_g=0.43), (c) Without proposed control (R_g/X_g=0.29), (d) With proposed control (R_g/X_g=0.29).

In this section, the experiments are developed to demonstrate the proposed analysis framework as well as the proposed virtual inductance control strategy. In Fig. 16, StarSim experimental setups include: oscilloscope, host PC, Rapid control prototype (RCP), IO board, and Hardware-in-the-loop (HIL) model. The RCP upload the controller built in the matlab Simulink model. And the HIL is connected to the hardware of the Simulink model. The HIL-RCP based StarSim can validate the proposed control algorithm rapidly in real time. The parameters of grid impedance and virtual inductance in those cases are given in Table II.

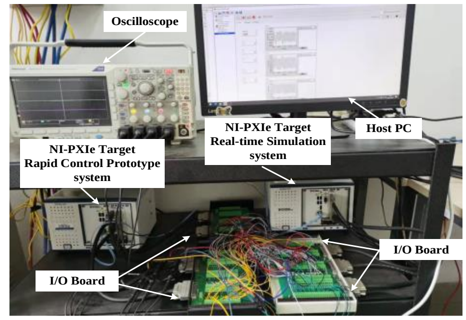

Fig. 16. StarSim experimental setups.

Fig. 17(a) and (b) show the experiment results of the frequency, grid-connected current, active- and reactive-power with the proposed virtual inductance method of case I. It shows that the system becomes unstable with disturbance of grid resistance R_g changed from 0.3 to 1.1 Ω, and a magnitude-equal oscillation occurs where the oscillation frequency is 101.5 rad/s, which validates the theoretical analysis. Compared to case I, a greater size of virtual inductance is introduced to test the effectiveness of control strategy in case II. In Fig. 17 (c) and (d), it can be seen that oscillation is attenuated much faster and convergence to equilibrium point with much faster response. It can be inferred that larger virtual inductance can provide more damping for the system to mitigate oscillation instability.

TABLE II PARAMETERS OF GRID IMPEDANCE AND VIRTUAL INDUCTANCE

Condition	Before			After		
Parameters	R_g/Ω	L_g/mH	L_v/mH	R_g/Ω	L_g/mH	L_v/mH
Case I	0.3	8.8	0	1.1	8.8	4.4
Case II	0.3	8.8	0	1.1	8.8	8.8
Case III	0.3	8.8	0	1.2	8.8	4.4

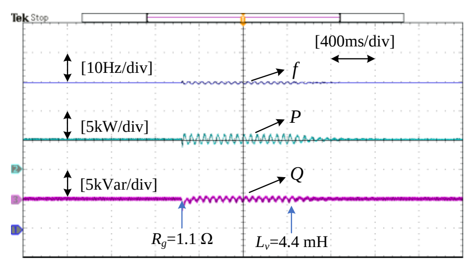

(a)

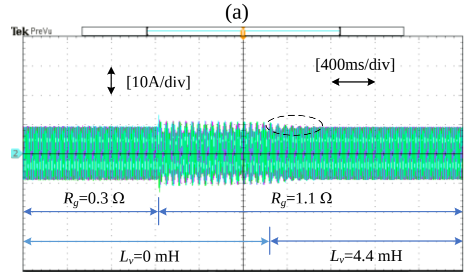

(b)

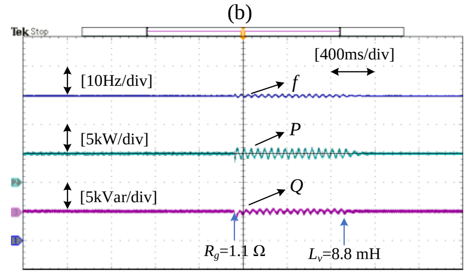

This article has been accepted for publication in a future issue of this journal, but has not been fully edited. Content may change prior to final publication. Citation information: DOI 10.1109/TIE.2022.3148749, IEEE Transactions on Industrial Electronics

(c)

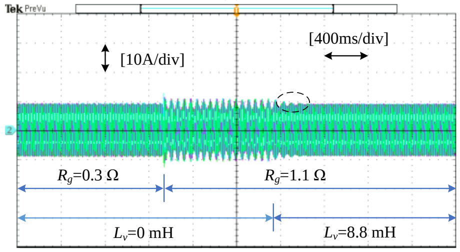

(d)

Fig. 17. Experiment results of P, Q, f and i_{abc} with different L_v. (a) Power and frequency waveforms with L_v=4.4 mH. (b) Grid-connected current waveform with L_v=4.4mH. (c) Power and frequency waveforms with L_v=8.8 mH. (d) Grid-connected current waveform with L_v=8.8 mH.

As for case III, Fig. 18 shows that the greater R_g results in larger magnitude of oscillation. With the virtual inductance control strategy put into operation, oscillation of the system gets convergent and finally be stable at an equilibrium point. It can be inferred that the proposed virtual inductance can provide damping support, mitigate the coupling effect between active- and reactive-power, and improve stability margins of the grid-forming VSG system. However, the transient response is lower by comparing to case II, it indicates that the higher power coupling would decrease the speed of stable recovery.

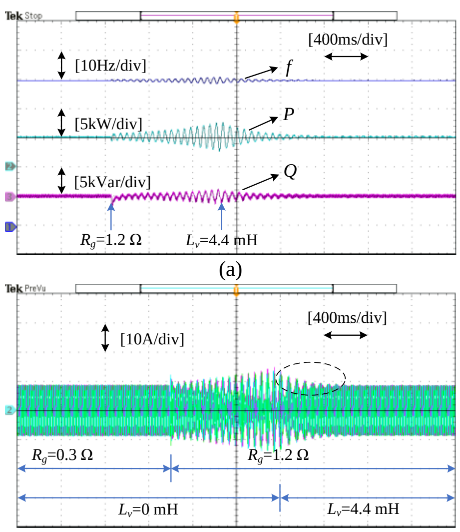

(b)

Fig.18 Experiment results of P, Q, f and i_{abc} of case III. (a) Power and frequency performance. (b) Grid-connected current.

V. Conclusion

This study established small-signal closed-loop active power model, which is used for identification of frequency stability of grid-forming VSG system. It is shown that the VSG system has a risk of oscillation instability due to negative damping, and it can be eliminated by the proposed virtual inductance control method. Besides, a new coupling model was developed to clarify the dynamic interaction between voltage magnitude and frequency of the system. By judging the size of feedback effect factor (FEF), motion trajectory of rate of change of frequency (RoCoF) and frequency offset (FO) can be known. Specifically, when the size of FEF is below one, it forms negative feedback that can stabilize system, and both RoCoF and FO finally tend to be zero, vice versa. Moreover, a new virtual inductance control strategy was proposed to dampen oscillation of grid-forming VSG by increasing positive damping power, and the effectiveness is validated by the FEF analysis. In this framework, it does not rely on dual-loop control structure, which is different from the conventional virtual inductance control. What's more, it is implemented based on energy conservation, and it can be adaptive to the power converter with another types of filters, like LC filters, and LCL filters. Besides, the LC filter is as similar as that of LCL filter since that the grid-side L filter of LCL filter can be integrated into the grid impedance as a whole. All of the analytical results of established models agree with the results of eigenvalue analysis. Finally, both proposed analytical model and virtual inductance control are verified experimentally.

Appendix

Combining (4.a) and (5.a) yields

$$P_{ref} - f(\delta_e, E) = D_p(\omega_e - \omega_n) + J_p\omega_n(\omega_E - \omega_n)s \quad \text{(A1)}$$

Linearizing (4.c), (A1) and combining (6), then (A2) can be obtained

$$\begin{aligned} &\Delta P_{ref} - (G_{P\delta}(s)\frac{1}{s}\Delta\omega_e + G_{PE}(s)\Delta E) \\ &= D_p(\Delta\omega_e - \Delta\omega_n) + J_p\omega_n s(\Delta\omega_e - \Delta\omega_n) \end{aligned} \quad \text{(A2)}$$

According to (A2), the relationship from ΔE to $\Delta\omega_e$ can be derived as

$$M_{\omega E}(s) = \frac{\Delta\omega_e}{\Delta E} = \frac{-G_{PE}(s)/(J_p\omega_n s + D_p)}{\left[1 + G_{P\delta}(s)/(J_p\omega_n s^2 + D_p s)\right]} \quad \text{(A3)}$$

Similarly, combining (4.b) and (5.b) yields

$$Q_{ref} - g(\delta_e, E) = J_q(E - U_{ref})s \quad \text{(A4)}$$

Linearizing (4.c), (A4) and combining (6), then (A5) can be obtained

$$\Delta Q_{ref} - (G_{Q\delta}(s)\frac{1}{s}\Delta\omega_e + G_{QE}(s)\Delta E) = J_q(\Delta E - \Delta U_{ref})s \quad \text{(A5)}$$

According to (A5), the relationship from $\Delta\omega_e$ to ΔE can be derived as

$$N_{E\omega}(s) = \frac{\Delta E}{\Delta\omega_e} = \frac{-G_{Q\delta}(s)/J_q s^2}{1 + G_{QE}(s)/J_q s} \quad \text{(A6)}$$

References

[1] F. Blaabjerg, M. Liserre and K. Ma, "Power Electronics Converters for Wind Turbine Systems," *IEEE Transactions on Industry Applications.*, vol. 48, no. 2, pp. 708-719, March-April 2012.

[2] C. Li, Y. Yang, N. Mijatovic and T. Dragicevic, "Frequency Stability Assessment of Grid-forming VSG in Framework of MPME with Feedforward Decoupling Control Strategy," in IEEE Transactions on Industrial Electronics. doi: 10.1109/TIE.2021.3099236

[3] Y. Yang, C. Li, J. Xu, F. Blaabjerg and T. Dragičević, "Virtual Inertia Control Strategy for Improving Damping Performance of DC Microgrid With Negative Feedback Effect," *IEEE Journal of Emerging and Selected Topics in Power Electronics.*, vol. 9, no. 2, pp. 1241-1257, April. 2021.

[4] J. Fang, H. Li, Y. Tang, et al., "Distributed Power System Virtual Inertia Implemented by Grid-Connected Power Converters," *IEEE Transactions on Power Electronics.*, vol. 33, no. 10, pp. 8488-8499, Oct. 2018.

[5] M. Saeedian, B. Eskandari, S. Taheri, et al., "A Control Technique Based on Distributed Virtual Inertia for High Penetration of Renewable Energies Under Weak Grid Conditions," *IEEE Systems Journal*., vol. 15, no. 2, pp. 1825-1834, June. 2021.

[6] L. Huang et al., "An Adaptive Inertia Control to Improve Stability of Virtual Synchronous Machines Under Various Power Grid Strength," *2019 IEEE Power & Energy Society General Meeting (PESGM)*, Atlanta, GA, USA, 2019, pp. 1-5.

[7] D. Li, Q. Zhu, S. Lin, et al., "A Self-Adaptive Inertia and Damping Combination Control of VSG to Support Frequency Stability," *IEEE Transactions on Energy Conversion*., vol. 32, no. 1, pp. 397-398, March. 2017.

[8] J. Fang, P. Lin, H. Li, Y. Yang and Y. Tang, "An Improved Virtual Inertia Control for Three-Phase Voltage Source Converters Connected to a Weak Grid," *IEEE Transactions on Power Electronics*., vol. 34, no. 9, pp. 8660-8670, Sept. 2019.

[9] H. Wu et al., "Small-Signal Modeling and Parameters Design for Virtual Synchronous Generators," *IEEE Transactions on Industrial Electronics*., vol. 63, no. 7, pp. 4292-4303, July. 2016.

[10] C. Li, Y. Yang, Y. Cao, et al., "Frequency and Voltage Stability Analysis of Grid-forming Virtual Synchronous Generator Attached to Weak Grid," *IEEE Journal of Emerging and Selected Topics in Power Electronics*., doi: 10.1109/JESTPE.2020.3041698.

[11] C. Li, Y. Li, Y. Cao, et al., "Virtual Synchronous Generator Control for Damping DC-Side Resonance of VSC-MTDC System," *IEEE Journal of Emerging and Selected Topics in Power Electronics*., vol. 6, no. 3, pp. 1054-1064, Sept. 2018.

[12] M. Saeedian, R. Sangrody, M. Shahparasti, S. Taheri and E. Pouresmaeil, "Grid-Following DVI-Based Converter Operating in Weak Grids for Enhancing Frequency Stability," *IEEE Transactions on Power Delivery*., doi: 10.1109/TPWRD.2021.3059898.

[13] W. Wu et al., "Sequence-Impedance-Based Stability Comparison Between VSGs and Traditional Grid-Connected Inverters," *IEEE Transactions on Power Electronics*., vol. 34, no. 1, pp. 46-52, Jan. 2019.

[14] J. Guo et al., "Analysis and Mitigation of Low-Frequency Interactions Between the Source and Load Virtual Synchronous Machine in an Islanded Microgrid," *IEEE Transactions on Industrial Electronics*., doi: 10.1109/TIE.2021.3075847.

[15] X. Liang, C. Andalib-Bin-Karim, W. Li, et al., "Adaptive Virtual Impedance-Based Reactive Power Sharing in Virtual Synchronous Generator Controlled Microgrids," *IEEE Transactions on Industry Applications*., vol. 57, no. 1, pp. 46-60, Jan.-Feb. 2021.

[16] Y. Hu, Y. Shao, R. Yang, et al., "A Configurable Virtual Impedance Method for Grid-Connected Virtual Synchronous Generator to Improve the Quality of Output Current," *IEEE Journal of Emerging and Selected Topics in Power Electronics*., vol. 8, no. 3, pp. 2404-2419, Sept. 2020.

[17] G. Lou, Q. Yang, W. Gu, et al., "Analysis and Design of Hybrid Harmonic Suppression Scheme for VSG Considering Nonlinear Loads and Distorted Grid," *IEEE Transactions on Energy Conversion*, doi: 10.1109/TEC.2021.3063607.

[18] P. Kundur, Power System Stability and Control. New York: McGrawHill, 1994.

[19] K. Wang and X. Yuan, "Stability Analysis of the Virtual Inductance for LCL Filtered Droop-controlled Grid-connected Inverters," *IEEE Journal of Emerging and Selected Topics in Power Electronics*., doi: 10.1109/JESTPE.2021.3058810.

[20] Y. Hu, Y. Shao, R. Yang, et al., "A Configurable Virtual Impedance Method for Grid-Connected Virtual Synchronous Generator to Improve the Quality of Output Current," *IEEE Journal of Emerging and Selected Topics in Power Electronics*, vol. 8, no. 3, pp. 2404-2419, Sept. 2020.

Yaqian Yang received the Master degree in Electrical Engineering from the Changsha University of Science and Technology in 2018. And she is pursuing Ph.D degree in Hunan University since 2018.
Her current research interests includes: stabilization and control of grid-forming virtual synchronous generators, synthetic inertial applied in hybrid AC/DC microgrids.

Jiazhu Xu was born in Chuzhou, China, in 1980. He received the B.S., M.S., and Ph.D. degrees in electrical engineering from Hunan University, Changsha, China, in 2002, 2004, and 2007, respectively. Since 2008, he has been an Associate Professor with the College of Electrical and Information Engineering, Hunan University, where he became a Professor in 2017. His current research interests include AC/DC power conversion theory, locomotive traction power supply systems, and optimization of modern electrical equipments.

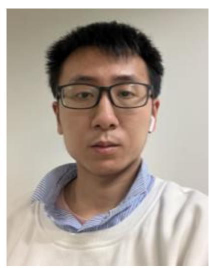

Chang Li received the Bachelor degree and the Ph.D. degree in Electrical Engineering from the Guizhou University and Hunan University in 2014 and 2020, respectively. Since October of 2020 he has been a Postdoc researcher at Technical University of Denmark.
His current research interests include: Power electronics interfaced power systems.

Weiming Zhang received Bachelor degree in electrical engineering and automation from Jiangsu University and Master degree in Electrical Engineering from the Hunan University in 2019 and 2021, respectively. Since 2021, he has been with Shenzhen Power Supply Co., Ltd. His current research interest includes design and control of DC distribution system.

This article has been accepted for publication in a future issue of this journal, but has not been fully edited. Content may change prior to final publication. Citation information: DOI 10.1109/TIE.2022.3148749, IEEE Transactions on Industrial Electronics

Qiuwei Wu (M'08-SM'15**)** obtained the PhD degree in Power System Engineering from Nanyang Technological University, Singapore, in 2009.

He was a senior R&D engineer with Vestas Technology R&D Singapore Pte Ltd from Mar. 2008 to Oct. 2009. He was working at Department of Electrical Engineering, Technical University of Denmark (DTU) from Nov. 2009 to Aug. 2021 (PostDoc Nov. 2009-Oct. 2010, Assistant Professor Nov. 2010-Aug. 2013, Associate Professor Sept. 2013-Aug. 2021). He is a tenured Associate Professor with Tsinghua-Berkeley Shenzhen Institute, Tsinghua Shenzhen International Graduate School, Tsinghua University. He was a visiting scholar at the Department of Industrial Engineering & Operations Research (IEOR), University of California, Berkeley, from Feb. 2012 to May 2012 funded by the Danish Agency for Science, Technology and Innovation (DASTI), Denmark. He was a visiting professor named by Y. Xue, an Academician of the Chinese Academy of Engineering, at Shandong University, China, from Nov. 2015 to Oct. 2017. He was a visiting scholar at the School of Engineering and Applied Sciences, Harvard University from Nov. 2017 – Oct. 2018 funded by the Otto Mønsted Fond.

His research interests are decentralized/distributed optimal operation and control of power systems with high penetration of renewables, including distributed wind power modelling and control, decentralized/distributed congestion management, voltage control and load restoration of active distribution networks, and decentralized/distributed optimal operation of integrated energy systems. He is an Editor of IEEE Transactions on Power Systems and IEEE Power Engineering Letters. He is also the deputy editor-in-chief and an Associate Editor of International Journal of Electrical Power and Energy Systems, and Journal of Modern Power Systems and Clean Energy. He is a subject editor for IET Generation, Transmission & Distribution, and IET Renewable Power Generation.

Ming Wen was born in Hubei, China, 1981. He received his M.S. degree and Ph.D. degree from Hunan University in 2006 and 2010, respectively. He has been a senior engineer at State Grid Hunan Electric Power Company Limited Economical & Technical Research Institute. His research interests include energy internet demand forecasting, electricity price, smart grid, renewable energy accommodation and power system planning.

Frede Blaabjerg (S'86–M'88–SM'97–F'03) was with ABB-Scandia, Randers, Denmark, from 1987 to 1988. From 1988 to 1992, he got the PhD degree in Electrical Engineering at Aalborg University in 1995. He became an Assistant Professor in 1992, an Associate Professor in 1996, and a Full Professor of power electronics and drives in 1998. From 2017 he became a Villum Investigator. He is honoris causa at University Politehnica Timisoara (UPT), Romania and Tallinn Technical University (TTU) in Estonia.

His current research interests include power electronics and its applications such as in wind turbines, PV systems, reliability, harmonics and adjustable speed drives. He has published more than 600 journal papers in the fields of power electronics and its applications. He is the co-author of four monographs and editor of ten books in power electronics and its applications.

He has received 33 IEEE Prize Paper Awards, the IEEE PELS Distinguished Service Award in 2009, the EPE-PEMC Council Award in 2010, the IEEE William E. Newell Power Electronics Award 2014, the Villum Kann Rasmussen Research Award 2014, the Global Energy Prize in 2019 and the 2020 IEEE Edison Medal. He was the Editor-in-Chief of the IEEE TRANSACTIONS ON POWER ELECTRONICS from 2006 to 2012. He has been Distinguished Lecturer for the IEEE Power Electronics Society from 2005 to 2007 and for the IEEE Industry Applications Society from 2010 to 2011 as well as 2017 to 2018. In 2019-2020 he served as a President of IEEE Power Electronics Society. He has been Vice-President of the Danish Academy of Technical Sciences. He is nominated in 2014-2020 by Thomson Reuters to be between the most 250 cited researchers in Engineering in the world.